International Journal of Refractory Metals and Hard Materials 140 (2026) 107883

Contents lists available at ScienceDirect

International Journal of Refractory Metals and Hard Materials

journal homepage: www.elsevier.com/locate/IJRMHM

Laser Directed Energy Deposition of Stellite 21-WC/Co coatings: processability, microstructure and dry-sliding wear behavior

Chiara Gianassi [a,*], Gianluca Di Egidio [b], Erica Liverani [a], Alessandro Fortunato [a]

[a] Department of Industrial Engineering (DIN), University of Bologna, Viale del Risorgimento, 2, 40136 Bologna, BO, Italy
[b] Department of Industrial Engineering (DIN), University of Bologna, Viale del Risorgimento, 4, 40136 Bologna, BO, Italy

ARTICLE INFO

Keywords:
Laser Directed Energy Deposition (L-DED)
Metal matrix composites (MMC)
Tribological performance
Stellite 21
WC/Co
Microstructure refinement

ABSTRACT

Laser Directed Energy Deposition (L-DED) is an effective technique for repairing and surface-engineering of components subjected to severe wear, enabling localized control of surface properties and extended service life. In this study, Stellite 21–based metal matrix composite (MMC) coatings reinforced with WC/Co 88/12 were deposited by L-DED on AISI 316 L steel, systematically varying the WC/Co content up to 30 wt% to investigate process–microstructure–property relationships.

Deposition parameters were tailored for each Stellite 21 + WC/Co composition to ensure coating integrity. Crack-free coatings with relative densities above 99% were achieved for reinforcement contents up to 20 wt% WC/Co, identifying this range as optimal. The coatings exhibit a refined CoCr-based dendritic/cellular matrix with an increasing fraction of eutectic constituents containing ultrafine carbides as WC/Co content increases, rather than WC agglomerates. This microstructure leads to a significant improvement in mechanical properties, with hardness values exceeding 800 HV1 for the 20 wt% WC/Co coating.

Tribological behavior was evaluated under dry sliding conditions against AISI 52100 in a block-on-ring configuration for coatings containing up to 20 wt% WC/Co. Results show a systematic reduction in both friction coefficient and wear depth with increasing WC/Co content. Notably, the Stellite 21 + 20 wt% WC/Co coating exhibits an approximately 90% reduction in wear depth compared to unreinforced Stellite 21. These results highlight the correlation between WC/Co-induced microstructural refinement and enhanced tribological performance, demonstrating the potential of L-DED-processed Stellite 21-based MMC coatings for advanced wear-resistant applications.

1. Introduction

In several industrial fields, such as agriculture, oil & gas, and tooling [1,2], components are required to operate under highly demanding conditions, including intense wear and exposure to corrosive environments. In these applications, performance is primarily governed by surface properties. Tools operating in severe tribological environments are often exposed to abrasive particles and mechanical contact. In many industrial applications, such components are produced through conventional manufacturing processes and replaced once damaged, leading to material waste and increased environmental impact [3]. A promising approach to mitigate this issue is the application of localized wear-resistant coatings on the most critical regions, enabling a significant extension of component service life while reducing production costs and resource consumption. Furthermore, when the coating process is sufficiently fast, flexible, and cost-effective, worn surfaces can be re-coated, further extending component lifetime and promoting a more sustainable use of materials. Comparable surface engineering strategies are being explored, for example, for brake discs, which are subjected to complex tribological and thermomechanical loading [4,5].

Laser Directed Energy Deposition (L-DED) technology, also known as laser cladding, is particularly well suited for these surface engineering applications, since it enables the localized deposition of coatings on critical regions of the component. In particular, powder-fed L-DED configurations provide a high degree of compositional flexibility through the use of multiple powder feeders, allowing the production of multi-material coatings, functionally graded materials and metal matrix composites (MMCs) without cross-contamination [6,7].

MMCs are materials consisting of a continuous metal matrix and a hard ceramic or refractory metal reinforcement [3,8]. Their growing

* Corresponding author.
E-mail address: chiara.gianassi2@unibo.it (C. Gianassi).

https://doi.org/10.1016/j.ijrmhm.2026.107883
Received 9 March 2026; Received in revised form 8 May 2026; Accepted 21 May 2026
Available online 22 May 2026

industrial relevance stems from their outstanding mechanical and tribological properties, which make them suitable for applications under critical working conditions [1]. As reported by [9], MMCs offer an excellent strength-to-weight ratio and high elastic modulus. This is attributed to the synergistic interaction between the matrix and the reinforcement, which restricts dislocation motion and limits plastic deformation through efficient load transfer.

Among metallic matrices for MMC coatings, cobalt-based alloys – particularly those known as Stellite alloys – are widely used due to their high mechanical strength, excellent wear resistance, and good corrosion and creep resistance [10]. Stellite 6 is the most commonly employed in industrial applications, owing to its high carbon content (> 0.8 wt%), which promotes the formation of hard carbides and ensures excellent wear resistance. However, the same high carbon and tungsten contents can increase the susceptibility to cracking during laser-based additive manufacturing processes, due to the formation of brittle carbides and the development of high residual stresses under rapid solidification conditions.

The tribological performance of Stellite-based coatings can be further enhanced by the addition of ceramic reinforcements such as WC/Co, which significantly increase hardness and wear resistance. Similar improvements have been widely reported also in other metal-ceramic systems, including WC-reinforced Ni-based coatings, where the combination of a ductile metallic matrix and hard ceramic particles provides an effective balance between toughness and wear resistance [11]. Nevertheless, the incorporation of WC/Co also introduces challenges, as it promotes brittleness and increases crack susceptibility, especially at high reinforcement contents [12].

Following initial studies focused on the optimization of L-DED processing of single materials, including Stellite alloys [10,13,14] and WC/Co systems [12], early investigations on MMC coatings mainly focused on depositing single tracks and correlating process parameters, microstructure, and mechanical properties [9,15].

In addition to microstructural aspects, particular attention has been devoted to the tribological performance of MMC coatings. Previous studies have demonstrated the potential of WC-reinforced coatings to improve tribological behavior, although the resulting performance strongly depends on both composition and processing conditions. Bartkowski et al. [16] reported a significant improvement in wear resistance for Stellite 6 coatings reinforced with 60 wt% WC deposited on S355 steel, while also highlighting a decrease in performance with increasing laser power. Similarly, Félix-Martínez et al. [17] investigated laser-cladded Stellite 6–WC-Co coatings deposited on AISI 304 and tested against an Al_2O_3 counterbody, reporting good wear resistance at both room and elevated temperatures. Other authors focused on the effect of WC addition in Stellite 6-based coatings. Ostolaza et al. [9] observed improved wear resistance in L-DED Stellite 6–WC coatings on AISI 1045 with increasing WC content up to 10 wt%. Similarly, Xu et al. [18] reported that the addition of 90 wt% WC to Stellite 6 resulted in an 18-fold improvement in wear resistance compared to the unreinforced alloy.

Despite the improved hardness and wear resistance achieved with WC reinforcement, several studies have highlighted critical limitations in Stellite-based MMC coatings. In particular, crack formation becomes increasingly pronounced when the WC content exceeds a critical threshold [18], severely compromising coating integrity and load-bearing capability. For instance, WC additions above 20 vol% in Stellite 6-based systems have been associated with a sharp increase in crack density and quasi-cleavage fracture behavior [2]. From a metallurgical standpoint, this issue is further exacerbated in matrices containing high amounts of tungsten and carbon, such as Stellite 6, where the formation of continuous brittle carbide networks and high residual stresses promotes crack initiation and propagation.

In this context, the selection of the matrix alloy becomes crucial to achieve a balance between wear resistance and processability. Stellite 21 represents a promising alternative, owing to its lower carbon content and higher molybdenum concentration, which favor the formation of more stable phases while reducing excessive carbide brittleness. This results in improved oxidation and corrosion resistance, as well as enhanced thermal stability and galling resistance, even at elevated temperatures [13]. These characteristics suggest that Stellite 21 could mitigate the crack susceptibility typically observed in Stellite 6-WC systems, while still benefiting from the reinforcement effect of WC/Co particles.

However, the available literature on L-DED MMC coatings based on cobalt alloys is almost exclusively focused on Stellite 6-based systems, while studies addressing other Co-based matrices are extremely limited. To the best of the authors' knowledge, no systematic investigations have been reported on Stellite 21–WC/Co MMC coatings, particularly with respect to their tribological behavior on steel substrates.

Therefore, the present research aims to investigate the microstructure and tribological behavior of Stellite 21-WC/Co coatings produced by L-DED. The process feasibility and repeatability were first assessed by systematically varying the WC/Co content from 0 to 30 wt% and optimizing the L-DED parameters for each reinforcement level. Subsequently, dry sliding wear tests in a block-on-ring configuration were conducted, and the resulting wear tracks were analyzed to elucidate the dominant wear mechanisms as a function of reinforcement content. The results highlighted the strong influence of WC/Co content on microstructure, hardness, and wear behavior, confirming the potential of Stellite 21–WC/Co MMCs as a process-stable, industrially viable solution.

2. Materials and methods

2.1. Materials

Coatings were deposited on 15 mm-thick AISI 316 L austenitic stainless-steel plates, selected for their widespread use in industrial applications and in laser-based additive manufacturing. Moreover, its good corrosion resistance and stable processing behavior ensure reliable, repeatable deposition conditions for the fabrication of wear-resistant coatings.

The depositions were produced using either pure atomized CoF75 powder or a mixture of CoF75 and WC/Co 88/12. CoF75, commercially known as Stellite 21, is a Co-based alloy containing dispersed hard carbides that enhance the wear and corrosion resistance. The powder was supplied by m4p (m4p Material Solutions GmbH, Feistritz i. R., Austria) with a particle size range of 45–106 μm. Reinforcement was provided by WC/Co particles with an average size of 53 ± 20 μm, produced by GTV (GTV Verschleißschutz GmbH, Luckenbach, Germany). Table 1 reports the chemical composition of the base material and both powders, assessed using a Field Emission Gun-Scanning Electron Microscope (FEG-SEM) with Energy-Dispersive X-ray Spectroscopy (EDS).

Based on the powders described above, four mixtures were prepared with WC/Co contents of 5 wt%, 10 wt%, 20 wt%, and 30 wt%. In addition, pure CoF75, without reinforcement, was included as a reference material in the study. The Co-based alloy and WC/Co powders were weighed using a Bonvoisin 5000 g × 0.01 g laboratory analytical balance, then manually mixed. A representative powder sample from each mixture was analyzed using FEG-SEM to assess the homogeneity and chemical composition of the blends (Fig. 1). The CoF75 powder produced by gas atomization exhibits a spherical, relatively uniform morphology. In contrast, the WC/Co particles show an irregular shape, as they are obtained through agglomeration and sintering of powder suspensions.

2.2. Experimental procedure

Specimens were produced using a Laser Directed Energy Deposition system with a 6-axis ABB IRB 4600 robot and an external 2-axis IRBP A250 roto-tilting positioner. The system features a Laserline LDF-4500-60 diode laser with a maximum output power of 4.5 kW. The deposition

Table 1
Chemical composition of the particles of CoF75 and WC/Co 88/12 and AISI 316L evaluated through FEG-SEM EDS.

[wt%]	W	Co	Cr	Mo	Mn	Si	Ni	C	Fe	N
AISI 316L	–	–	18.58	0.44	1.69	0.44	8.40	0.02	Bal.	0.11
CoF75- Stellite 21	–	Bal.	28.45	5.45	0.08	0.77	0.10	0.10	0.08	0.25
WC/Co 88/12	Bal.	12.30	–	–	–	–	–	5.50	–	–

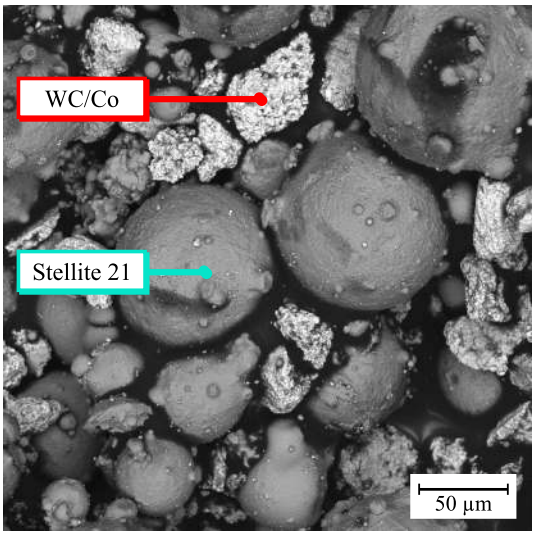

Fig. 1. FEG-SEM image of the Stellite powder mixed with 30 wt% WC/Co.

head is a Laserline OTS-5 with a collimating distance of 80 mm and a focusing length of 300 mm, resulting in a final spot diameter on the workpiece of 2.2 mm. The system is equipped with a feeding fiber with a 600 µm core diameter. The powder delivery system includes a GTV PS2/2 feeder and a 6-way GTV PN6625 nozzle with a standoff distance of 25 mm and a powder jet focus of 2 mm. Argon was used as carrier and shielding gas, with flow rates of 7.5 l·min^{-1} and 20 l·min^{-1}, respectively. A schematic of the deposition setup, along with the technical specifications of the laser source and powder feeder, is provided in Fig. 2.

The experimental workflow was structured into three main phases: specimen production, microstructural and mechanical characterization, and wear testing. A schematic overview of the entire experimental procedure is shown in Fig. 3, which visually summarizes the steps for each material and processing condition.

Five powder compositions were investigated: pure Stellite (CoF75) and Stellite reinforced with 5, 10, 20, and 30% WC/Co. For each composition, three different combinations of process parameters were tested. The cladding samples consisted of six-layer depositions with dimensions of 30 × 10 mm^2, fabricated using a zig-zag scan strategy. A hatch spacing of 1 mm was used, resulting in 50% overlap between adjacent tracks. The *Z*-direction increment was fixed at 1 mm, resulting in the deposition heights listed in Table 5.

Three sets of process parameters were evaluated:

- **Set A**: laser power of 1300 W, scanning speed of 780 mm·min^{-1}
- **Set B**: laser power of 2000 W, scanning speed of 1200 mm·min^{-1}
- **Set C**: laser power of 2400 W, scanning speed of 1320 mm·min^{-1}

All parameter sets were designed to provide an energy density of approximately 45–50 J·mm^{-2}, in accordance with the literature values reported for L-DED-printed WC/Co [13], Stellite 6 [19], and Stellite 6 + WC/Co [16,19]. The energy density *E* was calculated using the following equation (Eq. (1)):

$$E = \frac{P}{v \bullet D} \tag{1}$$

where *P* is the laser power [W], *v* is the translational speed of the nozzle, and *D* is the laser spot diameter [mm]. It should be noted that *v* must be

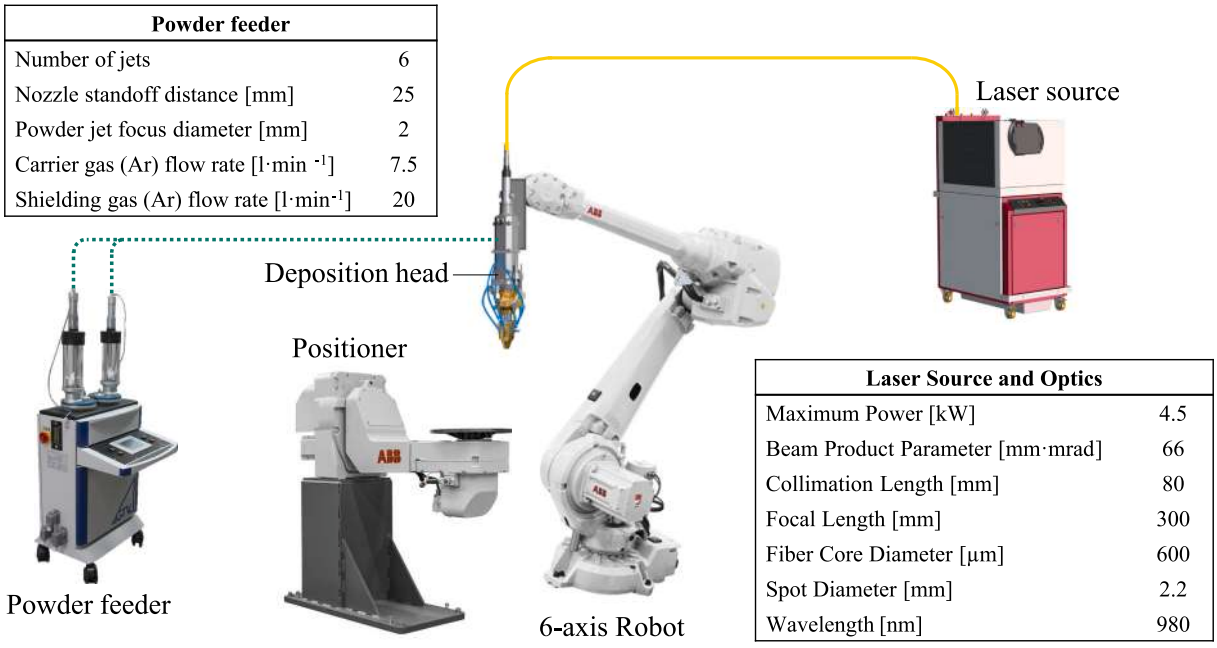

Fig. 2. Schematic representation of the L-DED setup used for the deposition process. The figure also includes the technical specifications of the laser source and powder feeding system.

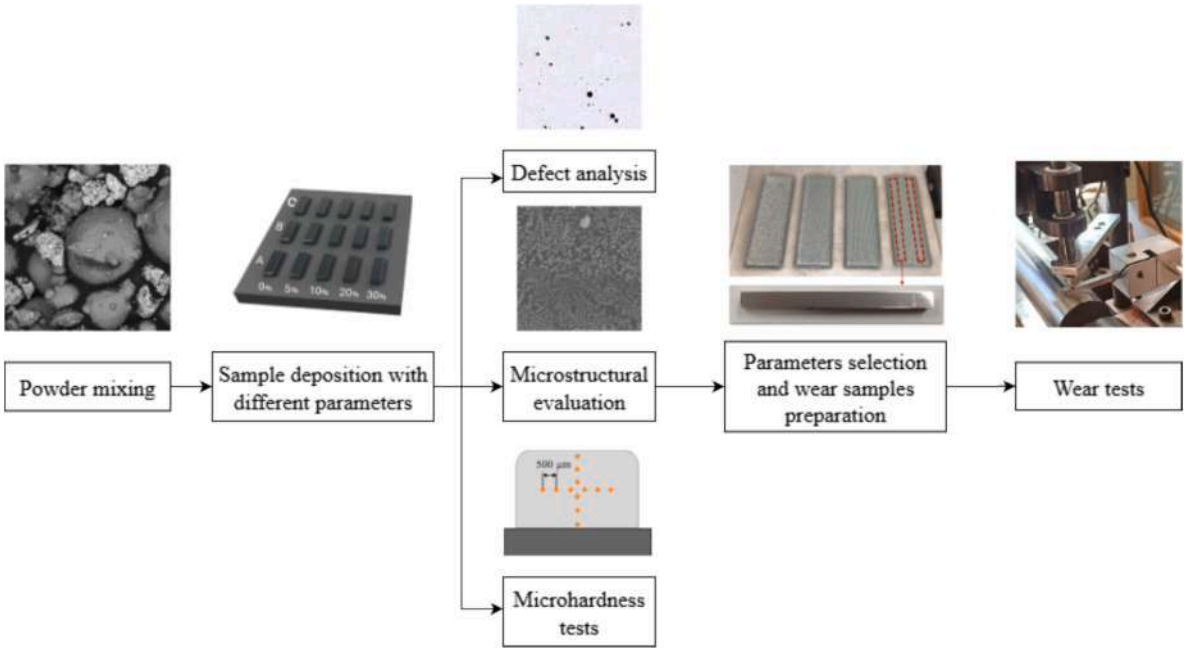

Fig. 3. Work flow of the experimental procedure.

expressed in mm·s^{-1} when used in Eq. (1). In this study, although the scanning speed is reported in mm·min^{-1}, it was converted into mm·s^{-1} for the calculation of *E*. Table 2 summarizes the full process conditions for each sample, using the nomenclature *"X##"*, where the letter *X* refers to the process parameter set (A, B, or C) and ## indicates the percentage of WC/Co reinforcement.

The powder feed rate, which depends on the mixture density and the rotational speed of the powder feeding system, was calibrated experimentally. The feeding system requires an input value expressed in rpm, which was manually set for each test. To determine the actual powder flow rate in grams per minute (g·min^{-1}) for each mixture and rpm value, the mass of powder delivered in 1 min was measured using a precision scale. This procedure was performed three times for each condition to ensure repeatability. The final flow rate values in g·min^{-1} were obtained by averaging the three measurements. Table 2 reports both the set rpm values and the corresponding converted flow rates in g·min^{-1}.

For Set A, a powder feed rate of 3 rpm was assigned. In comparison, a higher feed rate of 4 rpm was required for parameter sets B and C in 5, 10, 20, and 30 wt% samples to exceed the minimum theoretical mass flow rate g_{min}, calculated according to [13] using the following expression (Eq. (2)):

$$g_{min} = v \bullet t \bullet h \bullet \rho \quad (2)$$

where t is the layer thickness [mm], h the hatch spacing [mm], and ρ the mass density of the powder blend. The density of each mixture was estimated as a weighted average of the constituent percentages, using the known densities of Stellite 21 (8.33 g·cm^3) and WC/Co (17.11 g·cm^3) powders.

For the tribological tests, four different coatings (Table 3) containing 0, 5, 10, and 20 wt% WC/Co were fabricated using the optimized process

Table 3
Process parameters and WC/Co content of the specimens prepared for tribological tests.

Sample ID	Number of specimens	WC/Co content [wt%]	Laser power [W]	Scan velocity [mm·min^{-1}]	Powder flow rate [g·min^{-1}]
W0	2	0	2000	1200	10
W5	2	5	1300	780	11
W10	2	10	1300	780	11
W20	2	20	1300	780	13

Table 2
List of process parameters used for each test and the corresponding calculated energy densities.

Specimen	WC/Co content [wt%]	Power, P [W]	Scan velocity, v [mm·min^{-1}]	Feeder speed, g_{rpm} [rpm]	Powder flow rate, g [g·min^{-1}]	Energy density, E [J·mm^{-2}]
A0	0	1300	780	3	10	45.5
B0	0	2000	1200	3	10	45.5
C0	0	2400	1320	4	14	49.5
A5	5	1300	780	3	11	45.5
B5	5	2000	1200	4	14	45.5
C5	5	2400	1320	4	14	49.5
A10	10	1300	780	3	11	45.5
B10	10	2000	1200	4	14	45.5
C10	10	2400	1320	4	14	49.5
A20	20	1300	780	3	13	45.5
B20	20	2000	1200	4	14	45.5
C20	20	2400	1320	4	14	49.5
A30	30	1300	780	3	13	45.5
B30	30	2000	1200	4	15	45.5
C30	30	2400	1320	4	15	49.5

parameters identified in the preliminary phase of the study. Six layers were deposited for each condition on the 316 L substrate, resulting in a coating measuring 30 × 90 mm^2. Subsequently, two wear test specimens were extracted by wire-electro discharge machining (w-EDM), obtaining eight blocks (Fig. 3) with dimensions of 70 × 5 × 5 mm^3 (Ra = 0.4 ± 0.1 μm and Rq = 0.6 ± 0.1 μm, after grinding). No wear samples were produced with 30% WC/Co, as all parameter sets resulted in cracked, detached coatings.

2.3. Microstructural characterization and microhardness tests

For metallographic preparation, cross sections were extracted from the center of the deposits using w-EDM, mounted, and polished. Specimens with a maximum reinforcement of 10% WC/Co were ground using SiC sandpapers (80 to 2500 grit) and polished with a 1 μm alumina suspension. For the more complex samples with 20 wt% and 30 wt% WC/Co, the Aka-Grinding method was used, followed by polishing with diamond suspensions down to 1 μm.

All samples were initially examined using a Keyence VHX-7000 digital optical microscope to identify defects such as cracks and porosity. Cross-sectional images were analyzed in ImageJ to determine the relative density for each condition. Chemical etching was performed using two methods: (i) swabbing the surface with Murakami reagent for 10–30 s, depending on the WC/Co content, to highlight the segregation zones and the dendritic matrix, and (ii) electrochemical etching (4 V for 20 s) with an acidic ferric chloride solution (5 ml HCl + 10 g FeCl3 in 100 ml aqueous solution) to highlight the structure of the melt pool. Microstructural analysis was initially conducted via optical microscopy (Zeiss AXIO Observer A1m) and later using a scanning electron microscope (Tescan Mira3) equipped with an EDS detector (Bruker X-Flash 630 M) for more detailed elemental and morphological investigations.

Vickers microhardness measurements were performed in accordance with ISO 6507-1:2023 on polished cross-sections using a Remet HX-1000 microhardness tester. A load of 1 kg (HV1) was applied with a dwell time of 15 s. For each specimen, twelve indentations were performed: six along a vertical path and six along the horizontal direction, with 500 μm spacing, as schematically reported in Fig. 3.

2.4. Dry sliding tests

Tribological tests were performed to compare the coefficient of friction and wear resistance of the coatings. The specimens produced as described in Section 2.2 were subjected to dry sliding wear tests using a slider-on-cylinder tribometer in a block-on-ring configuration (Fig. 3), in accordance with ASTM G77-17 standard. The tribological system consisted of a stationary block specimen and an AISI 52100 steel cylinder (40 mm in diameter) used as the counterbody. The steel cylinder was quenched and tempered to a hardness of 62 HRC and exhibited a surface roughness of Ra = 0.15 ± 0.02 μm. Additional details regarding the tribometer configuration and experimental setup are reported in previous works by the authors [20,21]. The simplified contact geometry adopted in this laboratory-scale test allows for a direct comparison among the investigated conditions. The tests were conducted at a sliding velocity of 0.3 $m{\cdot}s^{-1}$ under ambient conditions (20–25 °C, relative humidity 50–60%), for a total sliding distance of 1000 m. Two normal loads, 30 N and 50 N, were applied to the stationary block. During the tests, the normal force, friction force, and vertical displacement were continuously monitored using bending load cells and a linear variable differential transformer (LVDT), respectively.

Assuming line contact between the two triboelements, the contact pressures were calculated using Hertzian contact theory for two parallel cylinders, with one body having an infinite radius to reproduce the block-on-ring contact geometry [22]. Under these assumptions, the maximum contact pressure can be expressed as follows (Eq. (3)):

$$P_{max} = \frac{(P \bullet E^{*})}{(\pi \bullet R)^{\frac{1}{2}}} \tag{3}$$

where P is the normal load for unit length, E^* is the contact modulus that considers Poisson's ratio and elastic modulus of the two facing materials, and R is the reduced radius of contact that considers the radius of both bodies. The mean contact pressure instead is defined as the following equation (Eq. (4)):

$$P_{mean} = \frac{\pi \bullet P_{max}}{4} \tag{4}$$

In the formula, an elastic modulus of 208 GPa for AISI 52100 was used [23]. The elastic modulus of the coatings was measured by nanoindentation tests with a Berkovich diamond indenter (centreline-face angle, α = 65.27°, Young's modulus, Eo = 1141 GPa, Poisson's ratio, νo = 0.07), according to the method reported in [24]. The Poisson's ratio of coatings was assumed to be 0.30, in accordance with commonly reported values for Co–Cr–Mo alloys [25]. Given the limited sensitivity of ν to microstructural variations, this assumption is considered appropriate for the present contact mechanics analysis. The nanoindentation tests were performed with a loading rate of 100 $mN{\cdot}min^{-1}$ and a holding time of 5 s at the peak load. The maximum load was set to 50 mN based on the penetration depth. For each condition, a 4 × 4 matrix of equally spaced indentations, spaced at 125 μm increments, was used. Given the limited variation among the measured values, an elastic modulus of 238 GPa was assumed for all coatings (W0, W5, W10, and W20), which is comparable with the value reported in the literature [25]. The peak and average contact pressures were reported in Table 4.

After testing, the worn surfaces of both the slider and the cylinder were characterized using 3D digital optical microscopy (Hirox KH-7700), axial chromatism confocal profilometry (Nanovea JR 25; Sensor: PS2; Magnifier: MG140; mapping area: 0.25 mm^2; scanning step: 2 μm; acquisition rate: 400 Hz), as well as FEG-SEM and EDS analysis, to identify the main wear mechanisms. Maximum wear depths, wear volumes and specific wear rates were calculated in accordance with ASTM G77-17 standard.

3. Results and discussions

3.1. Defect analysis

Table 5 summarizes the results of the cross-sectional analysis performed on each specimen, reporting the deposition height, relative density, and the presence of cracks, porosity, or interfacial delamination. The measured heights indicate that, across all reinforcement fractions and at a constant powder feed rate, increasing the laser power and scan speed reduced the overall build height. This behavior can be attributed to the shorter interaction time between the laser and the powder stream, which limits the amount of material effectively melted and incorporated into the melt pool, thereby reducing the vertical growth of the deposition.

Fig. 4 shows the evolution of defects as a function of process parameters and reinforcement content. For unreinforced Stellite, all parameter combinations yielded crack-free deposits with relative densities exceeding 99%. The best results were obtained with parameter set B (Fig. 4 – B0), while further increases in laser power and scan speed (set

Table 4
Hertzian contact pressures.

Contact parameters					
E [GPa]	ν	p_{max} [MPa]		$p_{average}$ [MPa]	
		30 N	50 N	30 N	50 N
238	0.3	108	139	85	109

Table 5
Measured deposition height, relative density, and occurrence of cracks, porosity, and interfacial delamination for each specimen.

Specimen	Deposition height h [mm]	Relative density ρ [%]	Defects
A0	6.60	99.30	Porosity
B0	4.62	99.65	Porosity
C0	5.66	99.15	Porosity
A5	7.09	99.71	Porosity
B5	6.11	97.17	Porosity
C5	5.62	96.74	Porosity
A10	6.83	99.33	Porosity
B10	5.92	97.82	Porosity
C10	5.55	96.10	Porosity
A20	5.84	99.37	Cracks
B20	6.84	99.78	Detachment
C20	5.33	99.84	Detachment
A30	7.99	99.40	Cracks-Detachment
B30	5.45	98.69	Cracks
C30	5.69	98.22	Cracks

C, Fig. 4 – C0) led to the formation of larger pores and a consequent decrease in density. A similar overall trend was observed for specimens reinforced with 5% and 10% WC/Co; however, the acceptable processing window shifted toward lower power levels. In fact, in both cases, parameter set A produced dense, crack-free coatings with relative density above 99% and only fine porosity (Fig. 4 – A5, A10). At higher laser powers and scanning speeds (sets B and C), porosity increased more markedly than in the unreinforced condition. The average pore size increased significantly, reaching values close to 1 mm, indicating greater sensitivity of the reinforced mixtures to excessive energy input (Fig. 4–B5, C5, B10, C10).

The increased porosity can be attributed to multiple concurrent mechanisms. A primary factor is the reduced flowability and packing density associated with the addition of irregular WC/Co particles to the otherwise spherical Stellite powder, which promotes gas entrapment during powder delivery and melting [26]. The presence of moisture in the powder can also lead to porosity; however, this mechanism is considered unlikely in the present case, as the powder was continuously stored in heated containers and the resulting pores do not exhibit preferential localization along melt pool boundaries, which is typically associated with moisture-related defects [27]. In addition, gas entrapment within the melt pool during processing is likely the dominant mechanism, particularly at higher laser power and scanning speeds,

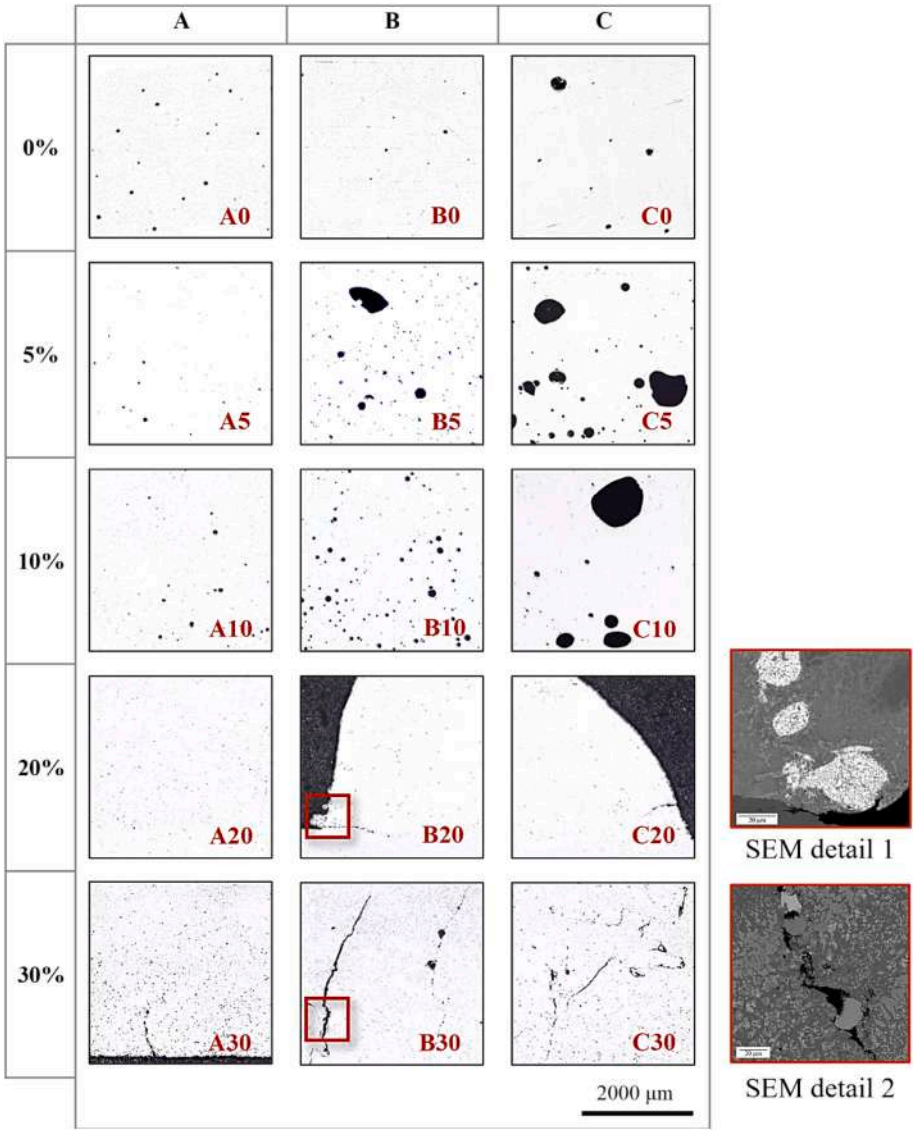

Fig. 4. Defect evolution as a function of process parameters (A–C) and reinforcement content (0–30% WC/Co), with representative micrographs. Corresponding SEM images highlighting specific defect features are reported on the right.

where increased melt pool turbulence and instability can enhance pore formation. The predominantly spherical morphology of the observed pores supports this interpretation. Larger cavities, exceeding the typical size of gas pores, are associated with the coalescence of trapped gas and local melt pool instabilities, possibly combined with incomplete wetting between the metallic matrix and ceramic reinforcement [26].

With a further increase in reinforcement content to 20 wt%, the nature of the defects changed: porosity became negligible, but cracks and partial delamination from the substrate were observed for sets B and C (Fig. 4 – B20, C20). Delamination can be ascribed to a combination of reduced dilution, local accumulation of carbide particles at the interface (Fig. 4 – SEM detail 1), and limited wettability between WC and the steel substrate, which together hinder the formation of a strong metallurgical bond. For specimens containing 30% WC/Co, cracks were consistently present in all conditions. The presence of spherical particles within crack paths (Fig. 4 – SEM detail 2) suggests incomplete melting or weak interfacial bonding, which may act as preferential sites for crack initiation and propagation. Finally, complete delamination was observed in Fig. 4 – A30. These findings suggest a critical reinforcement threshold for successful incorporation into the Stellite 21 matrix, likely between 20% and 30%.

3.2. Microhardness tests

Table 6 reports the average microhardness values and corresponding standard deviations obtained for the three-process parameter sets at different reinforcement fractions, distinguishing between horizontal (H) and vertical (V) indentation paths. No significant trends were observed between the two indentation directions. Conversely, the standard deviation increased with higher WC/Co content. This behavior, confirmed by [15], can be attributed to the intrinsic microstructural heterogeneity of the MMC at the indentation scale, as will be observed in the next section. Carbides precipitate mainly within the eutectic segregation zones of the microstructure; therefore, local variations in carbide density and in the dendritic/eutectic constituents lead to local hardness variations, as the microstructural features are affected by the indentations. As described in the next section, increasing the reinforcement fraction leads to a greater extent of eutectic regions, resulting in higher heterogeneity in the local constituent distribution and an increased hardness standard deviation.

Fig. 5 shows the average hardness trend as a function of the WC/Co content, for the three investigated parameter sets. For unreinforced specimens, hardness values were only marginally affected by the process parameters. All parameter sets produced dense coatings with porosity levels below 1% and no evident defects, resulting in low scatter and a relatively uniform hardness response.

At 5 wt%, 10 wt%, and 20 wt% WC/Co, specimens produced using the lowest laser power and scanning speed (set A) exhibited the highest average hardness and relative density. In the case of 10 wt% and 20 wt% WC/Co, the difference with respect to the other parameter sets exceeded 80 HV. Porosity may in principle influence hardness measurements by locally reducing the load-bearing area and increasing data scatter. In the present study, a decrease in average hardness was observed for processing conditions associated with higher porosity. However, this trend

Table 6
Average microhardness tests and standard deviations (HV) for different process parameters and reinforcement percentage, both for horizontal (H) and vertical (V) indentations.

		0%	*5%*	*10%*	*20%*	*30%*
A	V	411 ± 17	472 ± 11	597 ± 29	785 ± 56	869 ± 53
	H	386 ± 11	472 ± 6	560 ± 28	839 ± 88	871 ± 32
B	V	420 ± 16	463 ± 25	511 ± 30	689 ± 85	971 ± 63
	H	405 ± 10	451 ± 15	504 ± 16	686 ± 35	1004 ± 47
C	V	402 ± 14	464 ± 10	484 ± 17	731 ± 44	842 ± 63
	H	401 ± 10	466 ± 15	508 ± 38	686 ± 30	890 ± 74

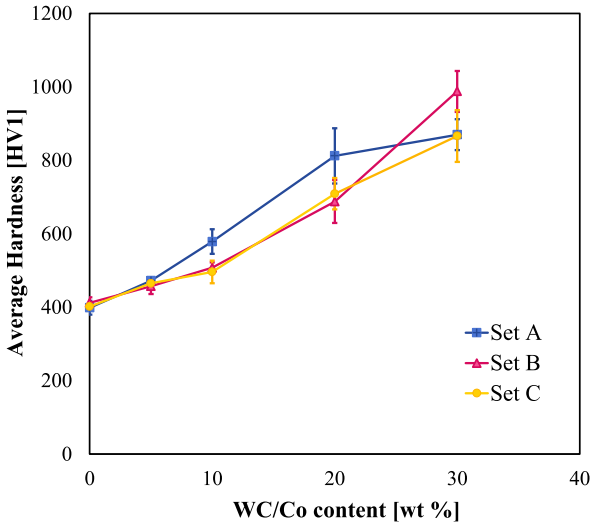

Fig. 5. Average Vickers microhardness as a function of WC/Co content and process parameter set.

is not accompanied by a significant increase in the standard deviation of the measurements, suggesting that the indentations were not directly affected by pores. Instead, the observed variations are more reasonably attributed to the influence of process parameters on the thermal cycles experienced during deposition, which govern matrix refinement and carbide formation. Although the reinforcement content remains the dominant factor controlling hardness, the processing conditions affect local solidification rates and cooling histories, leading to variations in the distribution and volume fraction of finely dispersed hard phases. Similar behavior was reported in the literature for Stellite–WC/Co MMCs, where process parameters were shown to influence hardness through their effect on thermal cycles and microstructural evolution [19].

Based on these findings, set B was selected for the unreinforced Stellite 21 coatings, as it provided the highest hardness and relative density, whereas set A was chosen for the 5 wt%, 10 wt%, and 20 wt% WC/Co composites, which consistently yield the highest hardness values. Since all parameter combinations led to coatings characterized by cracking and poor homogeneity at 30 wt% WC/Co, wear tests and further analysis were not conducted for this reinforcement level. Regardless of the potential wear performance, coating integrity represents a fundamental prerequisite for reliable functional behavior.

3.3. Microstructural analysis

Fig. 6 shows the influence of adding increasing WC/Co content on the microstructure of the Stellite 21-based coating. All coatings display the characteristic hierarchical microstructure induced by L-DED, comprising successive layers of solidified melt pools (Fig. 6a–d) that contain an oriented dendritic substructure (Fig. 6e–h). The multiple overlapping tracks that constitute the coating result in a non-uniform microstructure across the clad layers, due to the preferential growth orientation of the columnar dendrites, which is governed by the local heat flow direction (Fig. 6e–h). During deposition, the repeated melting and solidification associated with track overlap led to spatial variations in heat-flow direction and cooling rate within the melt pool, resulting in a heterogeneous microstructural morphology with features of varying sizes.

Fig. 7 illustrates the size and orientation of the microstructural features across the coated layer as a function of variations in the temperature gradient. Specifically, larger cellular dendrites form along the melt pool boundaries (MPBs) and near the clad-substrate interface (Fig. 7a–d), whereas finer columnar and cellular dendrites are observed

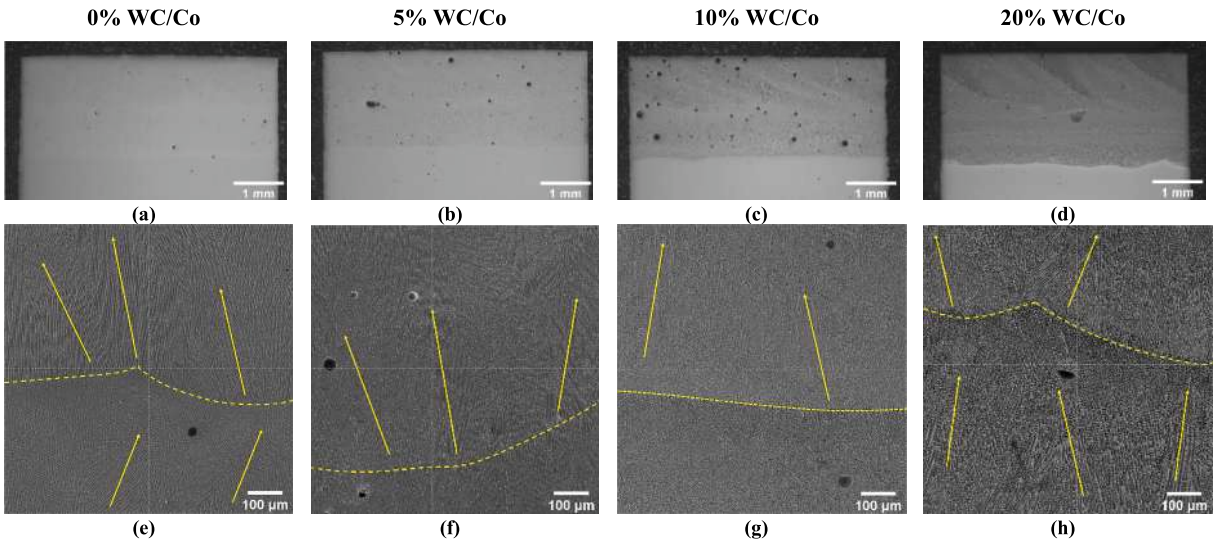

Fig. 6. OM (a-d) and FEG-SEM (e-h) images (Secondary Electron (SE)) images showing the microstructure of the coating with increasing %WC/Co content: (a,e) W0, (b,f) W5, (c,g) W10, (d,h) W20. Dotted lines: melt pool boundaries, yellow arrows: dendritic substructure orientation. (For interpretation of the references to colour in this figure legend, the reader is referred to the web version of this article.)

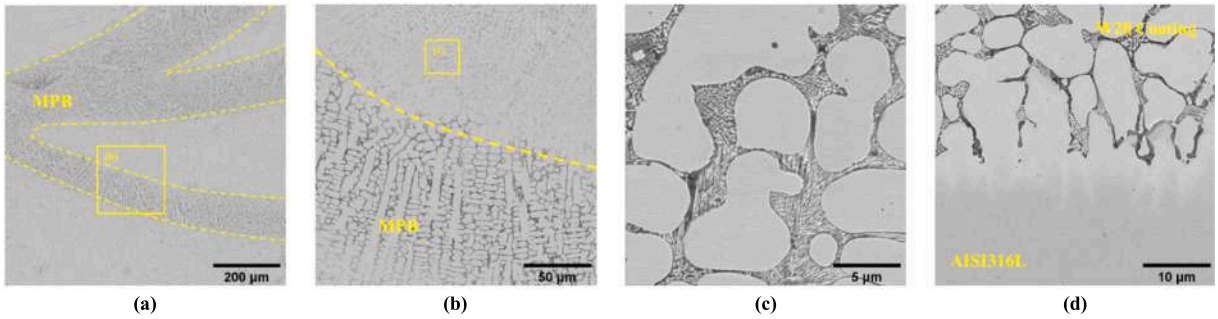

Fig. 7. BSE images of the CoCr dendritic matrix structure along the MPBs (a,c), the melt pool core (c), and at the substrate interface (d) of the W20 sample.

in the central region of the melt pool (Fig. 7b–c).

Fig. 6a–d highlights how the extent and distribution of segregation zones within the coating microstructure evolve with increasing WC/Co content. As the WC/Co fraction rises, both the size and spatial extent of the segregation zones (dark grey areas in Fig. 6) increase relative to the CoCr-based dendritic matrix (light grey areas in Fig. 6), resulting in an overall microstructural refinement. This effect becomes more evident upon examination of high-magnification micrographs: as shown in Fig. 8, increasing the WC/Co content from 0 to 20 wt% leads to a progressive enlargement of the eutectic regions and a concomitant refinement of the CoCr-based matrix. The microstructure evolves from a fully dendritic matrix containing isolated eutectic islands to a dendritic–cellular matrix embedded within a continuous eutectic constituent, in agreement with literature [9].

The EDS maps (Fig. 9) reveal the main microstructural constituents of the coatings, namely: (i) a CoCr-based dendritic matrix and (ii) a eutectic constituent located in the interdendritic regions. In particular, the CoCr-based matrix was found to be enriched in Ni, which remains trapped in solid solution due to diffusion-controlled phase transformations during rapid cooling, as also reported in [28]. The eutectic constituent consists of lamellae of a CoCr-rich phase (light grey areas in BSE image in Fig. 9) and ultrafine, homogeneously dispersed carbides

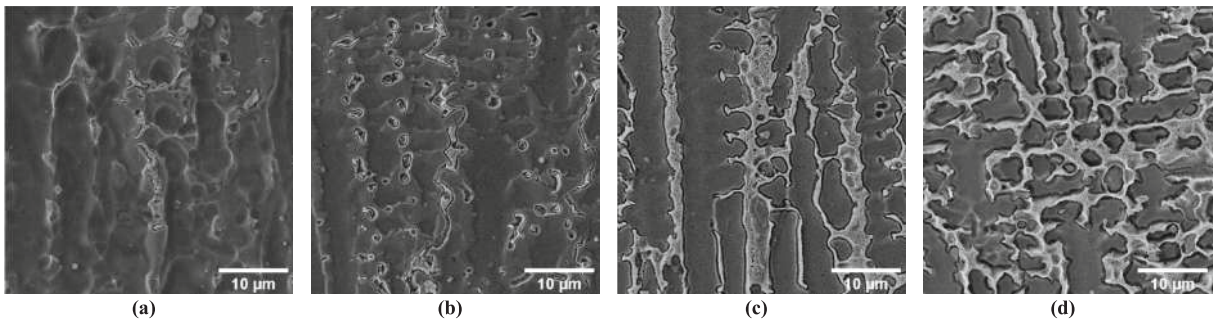

Fig. 8. SEM images show the variation in the CoCr-based matrix/segregation zone ratio with increasing WC/Co content: (a) W0, (b) W5, (c) W10, and (d) W20. The grey areas correspond to eutectic zones, while the black areas correspond to the Co–Cr–based matrix.

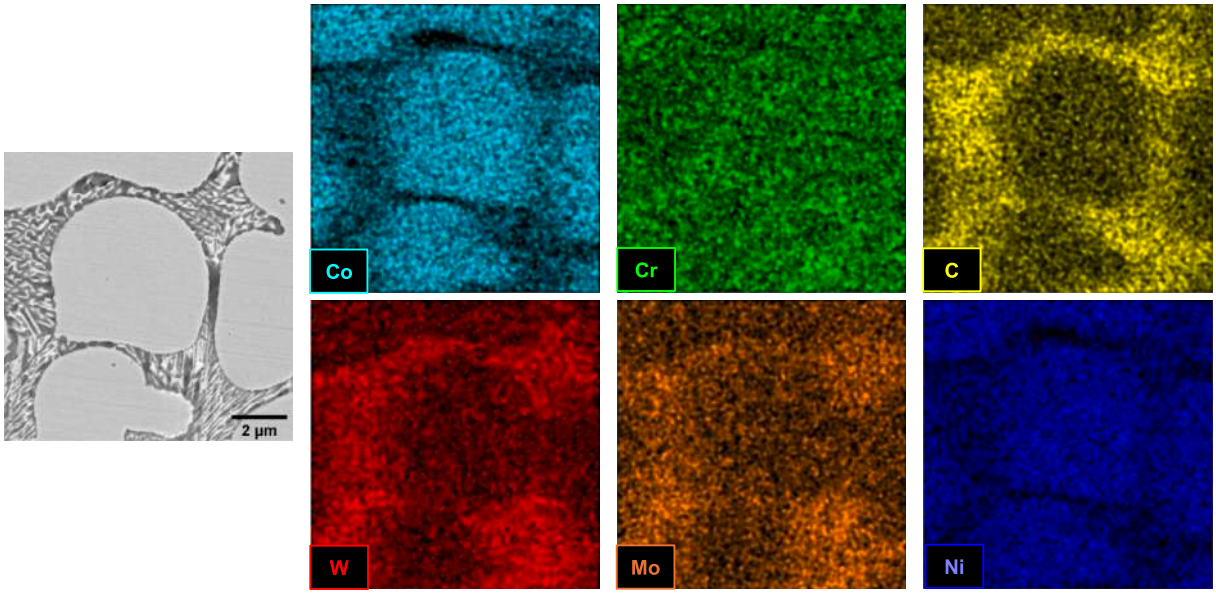

Fig. 9. BSE image (first) and EDS X-ray maps of the dendritic CoCr-based matrix structure and segregation zone in the 20%WC/Co coating.

(dark grey areas in BSE image in Fig. 9), as indicated by the enrichment in carbide-forming elements such as Cr, W, and Mo in EDS maps (Fig. 9). These microstructural features are consistent with previous studies [13,19,29]. The distinctive microstructure arises from the high solidification rates inherent to the L-DED process, which promote the redistribution of interstitial and substitutional elements within the melt pool and their subsequent partitioning at the solid–liquid interface. Under these conditions, carbide-forming elements preferentially segregate to the periphery of the dendritic–cellular matrix, where they form the carbides constituting the eutectic phase. In contrast, elements such as Ni are retained in solid solution within the matrix.

The higher microhardness measured in specimens with increased WC/Co content can be attributed to the enlargement of eutectic regions and to the higher density of ultrafine carbides within the segregation zones. As reported in [28], the solid solution of carbide-forming elements and C atoms, originating from the melting of Stellite 21 and WC/Co powders, promotes the formation and homogeneous dispersion of complex carbides, leading to enhanced hardness in Co-based alloys. During the coating process, these elements dissolve into the liquid Co matrix and subsequently form complex eutectic constituents through interdiffusion mechanisms within the melt pool. Furthermore, as reported in [30], newly formed eutectic carbides precipitate between dendrites, generating continuous, fine, and uniformly distributed lamellar networks (Fig. 9). It can therefore be reasonably assumed that this heterogeneous microstructure contributes not only to increased hardness but also to improved interfacial bonding and enhanced wear resistance of L-DED-deposited coatings. Notably, in contrast to other studies reported in the literature [15,17,19,31], the complete dissolution of WC/Co powders in the present work did not result in the retention of significant WC carbide residues. Instead, the enhanced hardness arises solely from the homogeneous dispersion of ultrafine carbides, which uniformly improve the mechanical properties of the coated layer across the whole surface.

Fig. 10 highlights the columnar growth of the coating microstructure at the interface with the substrate. EDS analysis (Fig. 10a) further reveals a significant decrease in Fe content from the coating–substrate interface (approximately 50 wt%) to the upper region of the first deposited layer (14.1 wt%), indicating adequate mixing between the first layer and the substrate, which is expected to enhance coating adhesion. The WC/Co content markedly influences microstructural development: as the WC/Co fraction increases, the extent of the segregation zones between dendrites increases, leading to a refinement of the matrix, which evolves from a fully columnar dendritic structure (Fig. 10a) to a columnar–cellular dendritic morphology (Fig. 10c).

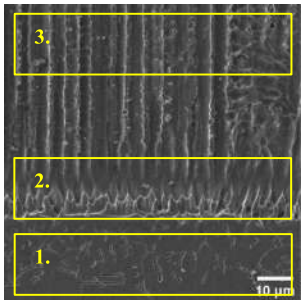

Wt.%	C	O	Cr	Fe	Co	W	Mo	Ni
1.	1.7	0.0	5.8	91.2	0.0	0.0	0.0	1.3
2.	3.5	1.5	24.3	50.0	19.8	0.7	0.2	0.0
3.	5.6	3.6	39.8	14.1	35.8	0.7	0.4	0.0

(a)

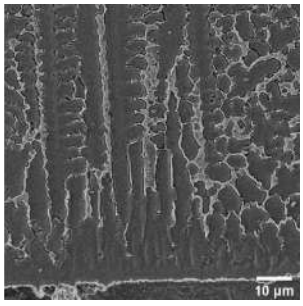

(b)

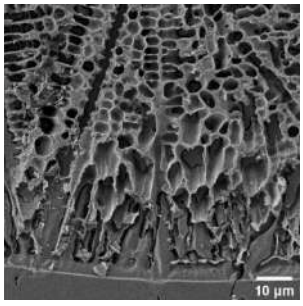

(c)

Fig. 10. SE images of the CoCr dendritic matrix structure at the substrate (AISI 316 L) interface: (a) W0, (b) W10, and (d) W20.

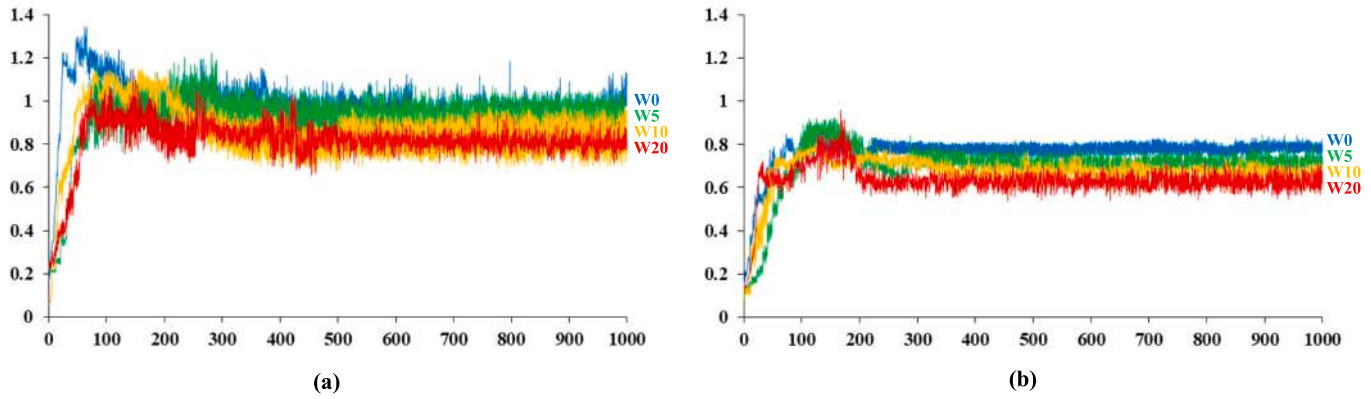

Fig. 11. Representative evolution of the CoF value as a function of sliding distance for: (i) W0, (ii) W5, (iii) W10, and (iv) W20. Applied normal load equal to 30 N (a) and 50 N (b).

3.4. Dry sliding tests

Fig. 11 displays representative plots of the coefficient of friction (CoF) as a function of sliding distance (sliding speed = 0.3 m·s^{-1}, total distance = 1000 m) obtained from dry-sliding wear tests performed on coatings with different WC/Co contents. Two normal loads (30 N and 50 N) were applied to better distinguish the tribological behavior of the various coating conditions. For each condition, the CoF trends were highly reproducible across the three repeated tests.

In all cases, the run-in stage is characterized by an initially low CoF (approximately 0.2), followed by a peak within the first 100–150 m. After this stage, CoF decreases due to frictional heating, which promotes the formation of oxide layers on the contact surfaces whose formation is documented by the images in Figs. 13–15, discussed in section 3.5. These layers act as solid lubricants [28], reducing the CoF until steady-state conditions are established after approximately 200 m.

Larger CoF oscillations and fluctuations are observed under the 30 N load (Fig. 11a). This behavior is associated with pronounced adhesive interactions and stick–slip phenomena, reflecting the cyclic formation, stabilization, and detachment of the oxide-based transfer layer on both the wear track and the counterbody during sliding. The increased fluctuations suggest that the tribolayer is less stable at 30 N than at 50 N (Fig. 11b), likely due to the lower contact pressure (Table 4), which hinders the formation of a continuous and stable oxide tribolayer. Nevertheless, for all tested loads and coating compositions, the CoF remains stable during the steady-state regime, indicating that the coatings can effectively sustain tribological contact without signs of failure, even in samples exhibiting lower hardness.

A comparison of the average steady-state coefficient of friction (CoF) values for coatings with different WC/Co contents is presented in Fig. 12a. The CoF decreases progressively from unreinforced Stellite 21 (W0) to Stellite 21 + 20 wt% WC/Co (W20). Specifically, at an applied load of 30 N, the CoF decreases from 0.97 to 0.82 (−15%), while at 50 N it decreases from 0.85 to 0.65 (−24%). The steady-state CoF values are consistent with those reported in the literature for Stellite 6/WC MMCs, notwithstanding the differences in the tribological systems adopted in the various studies [28,31].

The reduction in CoF with increasing applied load can be attributed to two concurrent mechanisms: (i) the formation of a thicker and more stable oxide tribolayer promoted by load-induced temperature increases, and (ii) an increase in the effective contact area, which enhances tribolayer adhesion, as described in [32]. As discussed previously, a more stable tribolayer, characterized by a low-shear third body (i.e., a oxidized debris-derived transfer layer), leads to less CoF fluctuations and lower average CoF values under steady-state conditions (Fig. 12b). In addition, the increase in coating hardness associated with higher WC/Co contents results in elevated local contact pressures and temperatures, further stabilizing the tribolayer by promoting the formation of a compact, adherent, and continuous low-friction oxide layer, thereby contributing to the CoF reduction (Fig. 12a).

As expected, the average wear depth (WD) decreases progressively from W0 to W20 under both applied loads (30 N and 50 N). At 30 N, the WC/Co-reinforced coatings (W5, W10, and W20) show relatively similar WD values, while W0 exhibits a markedly higher WD than W20 (+347%). Increasing the applied load to 50 N significantly amplifies the differences among the tested conditions, with the WD of W0 being up to 840% higher than that of W20. Consequently, a load of 50 N represented a more discriminating test condition for assessing the enhancement in wear resistance induced by higher WC/Co content.

By evaluating the wear volume according to ASTM G77-17, the wear

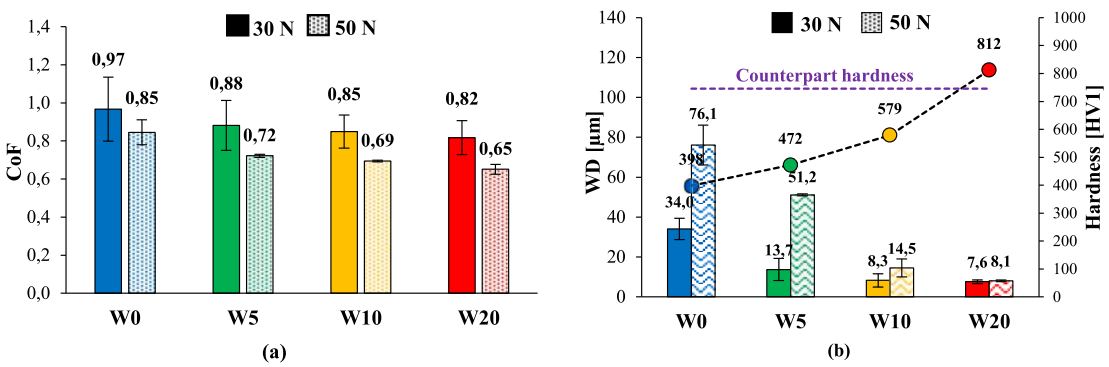

Fig. 12. Mean values of (a) steady-state CoF (CoF values were averaged from 200 to 1000 m range) and (b) WD versus hardness evaluated in the dry sliding test vs. 100Cr6 cylinder (counterpart).

Table 7
Wear volumes and specific wear rates evaluated according to ASTM G77-17 standard, related to different analyzed conditions: (i) W0, (ii) W5, (iii) W10 (iv) W20.

Coating conditions	Wear volume [mm^{-3}]x10^{-3}		Specific wear rate [mm^3/Nm]x10^{-6}	
	30 N	50 N	30 N	50 N
W0	229.7 ± 38.7	881.5 ± 83.2	7.66 ± 1.29	17.63 ± 1.66
W5	57.3 ± 18.8	122.7 ± 22.1	1.91 ± 0.63	2.45 ± 0.44
W10	19.5 ± 7.6	64.1 ± 6.9	0.65 ± 0.15	1.28 ± 0.14
W20	12.1 ± 1.4	28.9 ± 2.8	0.40 ± 0.01	0.58 ± 0.06

rate (Table 7) shows a significant decrease from W0 to W20 conditions. The inverse correlation between wear rate and hardness is consistent with Archard's law, which states that the wear volume is directly proportional to the applied load and inversely proportional to the material hardness [23]. As will be described in section 3.5, also the formation of a more stable tribo-layer, as well as the higher hardness, contributed to a reduced wear rate in W20 condition.

The results show a clear decrease in wear rate with increasing WC/Co content, mainly due to the higher hardness and improved load-bearing capacity of the coating associated with the refined microstructure discussed previously. This trend agrees with previous studies, although different tribological conditions were adopted. Xu et al. [18] reported a 3.5-fold reduction in specific wear rate for laser-cladded Stellite 6 reinforced with 20 vol% WC compared to unreinforced Stellite 6. Similarly, Ostolaza et al. [9] observed an approximately 30% increase in wear resistance when the WC content in Stellite 6-based MMCs increased from 5% to 10%.

A direct comparison with literature data remains difficult because

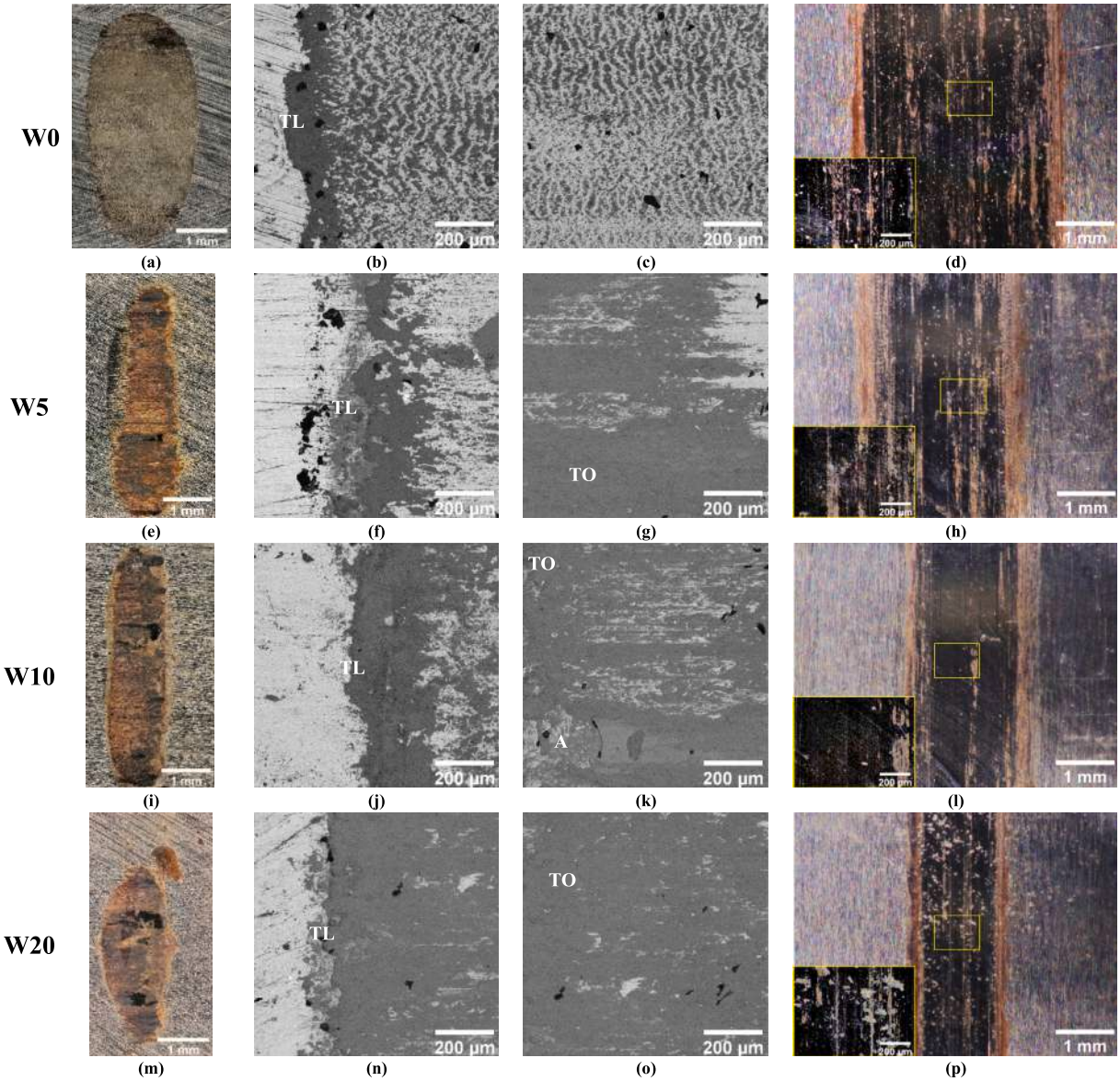

Fig. 13. 3D-digital optical and FEG-SEM images of the wear tracks of coated samples at 30 N test load: (a-c) W0, (e-g) W5, (i-k) W10, and (m-o) W20. 3D-digital optical images of the counterpart of coated samples at 30 N test load: (d) W0, (h) W5, (l) W10, and (p) W20. Labels indicate dominant wear mechanisms (TO = Tribo-oxidation; A = adhesion) or morphologies (TL: accumulation of wear debris transfer layer).

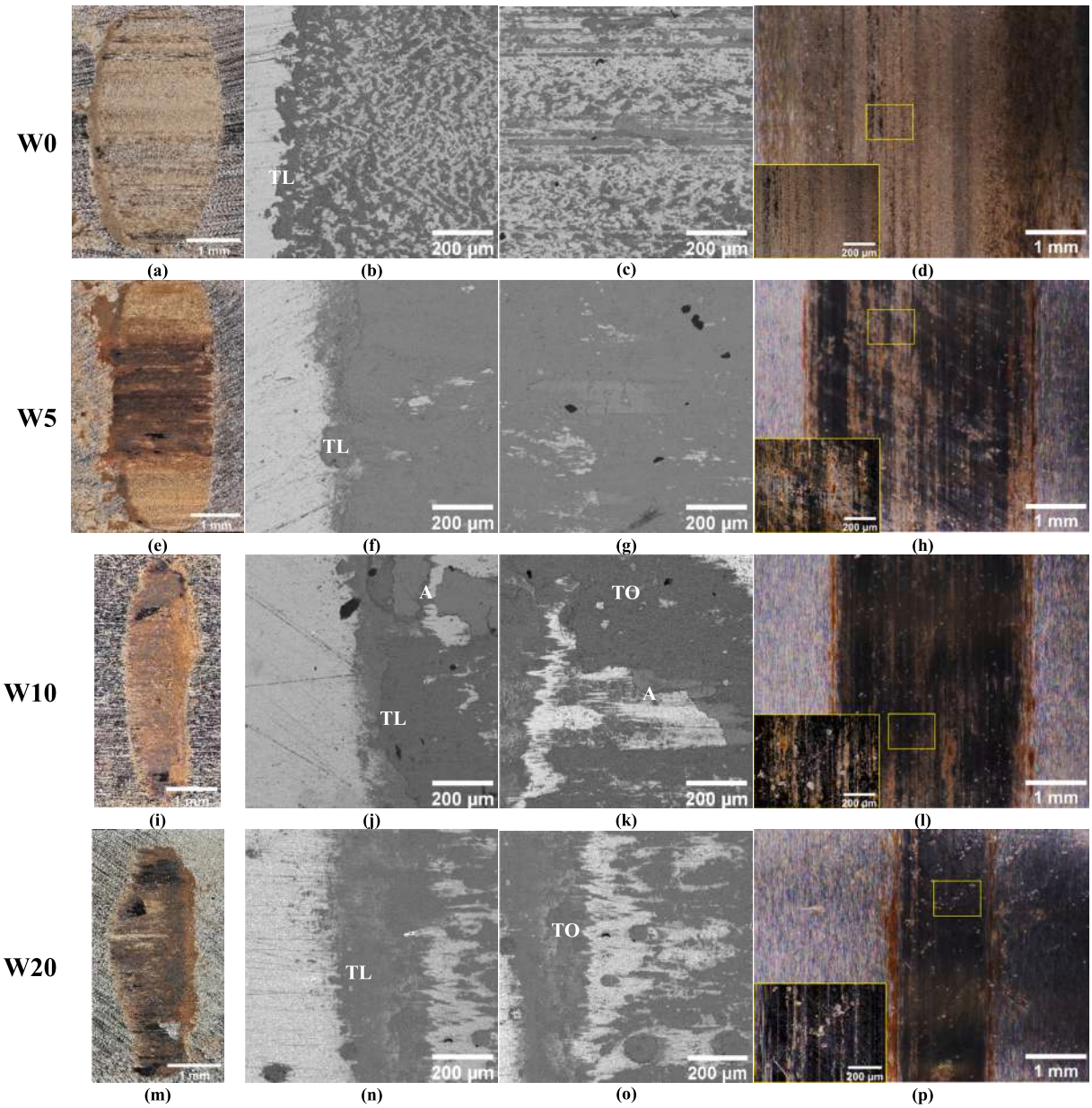

Fig. 14. 3D-digital optical and FEG-SEM images of the wear tracks of coated samples at 50 N test load: (a-c) W0, (e-g) W5, (i-k) W10, and (m-o) W20. 3D-digital optical images of the counterpart of coated samples at 50 N test load: (d) W0, (h) W5, (l) W10, and (p) W20. Labels indicate dominant wear mechanisms (TO = Tribo-oxidation; A = adhesion) or morphologies (TL: accumulation of wear debris transfer layer).

most studies employed different testing configurations, mainly ball-on-disk setups. Nevertheless, the reported wear rates are generally higher than those obtained in the present work. For example, Moshkbar Bakhshayesh et al. [28] measured specific wear rates between 19.7 × 10^{-6} and 49.1 × 10^{-6} mm^3/N·m for Stellite 6 sliding against 52,100 steel under loads from 10 to 50 N. Félix-Martínez et al. [17] reported wear rates in the range of 6.98 × 10^{-6}–12.71 × 10^{-6} mm^3/N·m for Stellite 6/WC-6Co coatings tested against an Al_2O_3 counterbody. Therefore, the specific wear rate measured for the Stellite 21 + 20 wt% WC/Co coating in the present work (0.58 ± 0.06 × 10^{-6} mm^3/N·m at 50 N) represents a remarkably low value. In addition to the increased hardness, this result can be related to the characteristics of the Stellite 21 matrix, whose lower carbon content and higher Mo concentration promote a more ductile microstructure with lower crack susceptibility than WC-reinforced Stellite 6 coatings.

3.5. Identification of wear mechanisms

Figs. 13 and 14 present in detail the wear tracks on the coated sliders and the cylindrical counterbody after dry sliding tests performed under applied loads of 30 N and 50 N, respectively.

The formation and accumulation of oxide-based transfer layers are clearly visible on the wear tracks of the coated sliders as dark grey regions in the BSE images (Figs. 13 and 14). Their high oxygen content, highlighted by the EDS analysis (Fig. 15 a,b), indicates the occurrence of a mild tribo-oxidative wear regime. Conversely, the bright grey regions observed in the same images are associated with localized material detachment caused by adhesive wear mechanisms.

The oxide-based tribolayer consists mainly of Fe-based compounds transferred from the 100Cr6 counterbody, together with Co- and Cr-based oxides originating from the coating. Its composition depends strongly on the relative hardness between coating and counterbody. For coatings with hardness lower than that of the counterbody (Fig. 15a),

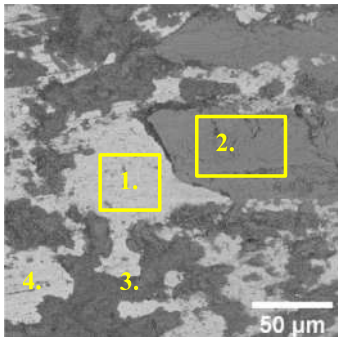

Wt.%	C	O	S	Cr	Fe	Co	W
1.	5.9	2.6	2.6	40.1	0.0	47.4	1.2
2.	3.0	42.2	0.0	18.0	16.3	20.5	0.0
3.	9.3	41.8	1.7	12.9	21.2	11.7	0.8
4.	2.6	3.1	4.0	42.2	3.9	43.7	0.5

(a)

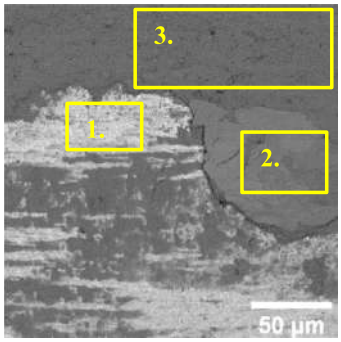

Wt.%	C	O	S	Cr	Fe	Co	W
1.	2.9	4.5	2.5	30.6	13.3	37.3	8.8
2.	2.0	29.8	0.0	2.1	66.1	0.0	0.0
3.	5.0	30.1	0.0	2.0	62.8	0.0	0.0

(b)

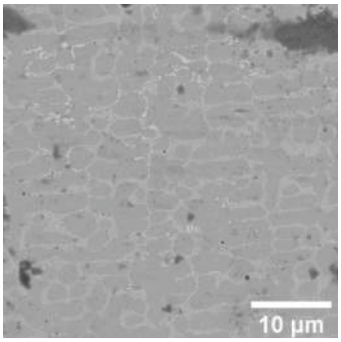

(c)

Fig. 15. BSE images and EDS analysis of the wear tracks of coated samples at 50 N test load: (a) W10, and (b) W20. (c) BSE image of zone 1 in (b) shows the CoCr-based cellular matrix structure embedded within a continuous eutectic constituent.

the tribolayer is predominantly formed by mechanically mixed oxides generated through the combined transfer of Fe-based oxides from the counterbody and Co-/Cr-rich debris detached from the coating. In contrast, when the coating hardness exceeds that of the counterbody (Fig. 15b), wear of the MMC-coated slider is significantly reduced, and the tribolayer is mainly composed of Fe-based oxides transferred from the counterbody, as confirmed by the higher Fe content detected by EDS. This behavior is consistent with the lower wear rates measured for the harder MMC coatings, suggesting that the oxide layer contributes to stabilizing the contact and reducing direct metal-to-metal interaction during sliding. Comparable results were reported by Ostolaza et al. [9] for Stellite 6/WC coatings, where the formation of Co- and Cr-based oxides was also observed. The authors also emphasized the protective function of the oxide tribolayer, which acts as a solid lubricating film, stabilizes the sliding contact, and thereby contributes to wear reduction.

Focusing on the wear tracks of the sliders, the oxide-based transfer layers exhibit a characteristic tribo-oxidative formation–disruption cycle. Flake-like debris produced by exfoliation of the low-shear-strength oxide layer after reaching a critical thickness was observed at the center of the wear track, whereas accumulation of compacted wear debris was mainly detected along the track edges (Figs. 13 and 14). Despite the local removal of the tribolayer, no significant microcracking of the coating was observed under the investigated conditions, indicating that the oxide layer mainly acts as a protective tribofilm. Its relatively uniform distribution over the sliding surface contributes to reducing both friction and wear by limiting direct metal-to-metal contact and functioning as a sacrificial layer progressively consumed during sliding. Once the oxide layer reaches a critical thickness, however, it undergoes fracture and spallation, exposing fresh material to renewed oxidation cycles (Fig. 15c), which is characteristic of tribo-oxidative wear mechanisms.

These observations are consistent with the findings of [28], who described a comparable cyclic tribo-oxidative process in Stellite 6-based coatings. In their study, the authors attributed the formation of the oxide films to frictional heating generated during sliding. The resulting oxide layers were locally removed under continued contact and subsequently re-formed in the newly exposed regions following tribolayer flaking. Furthermore, with increasing load up to 50 N, more extensive removal of the oxide layer and smoother worn surfaces were observed, in agreement with the behavior identified in the present work.

The partial removal of the transfer layer promoted localized direct contact between the slider and the cylindrical counterbody, resulting in a polishing effect that locally revealed the underlying coating microstructure. This behavior was particularly evident for the WC/Co-reinforced coatings, where the relatively high W content detected by EDS in Fig. 15b (Zone 1) reflects the high fraction of eutectic constituents in the 20 wt% WC/Co coating. Increasing the WC/Co content therefore not only enhances coating hardness and reduces wear, but also improves the load-bearing capacity of the coating through the combined effect of the eutectic matrix and finely dispersed carbides. These microstructural features provide more effective mechanical support to the oxide-based tribolayer, limiting its fragmentation and contributing to a lower coefficient of friction. Consequently, when the tribolayer is sufficiently adherent and adequately supported by the substrate, as in the reinforced coatings (W5, W10, and W20), its delamination is significantly reduced. Conversely, the lower load-bearing capability of the W0 coating promotes the formation of a discontinuous and poorly adherent oxide layer, resulting in less stable tribological behavior.

Examination of the wear tracks on the cylindrical counterbody (Figs. 13(d,h,l,p) and 14(d,h,l,p) reveals the presence of numerous

grooves parallel to the sliding direction, together with dark-brown, oxide-rich regions. These features indicate the coexistence of tribo-oxidative and adhesive wear mechanisms during dry sliding. Additionally, pronounced islands of detached material are observed on the counterbody surface due to material transfer to the opposing coated slider, characteristic of severe adhesive wear. Although direct SEM/EDS characterization of the counterpart was not performed, the presence of Fe-rich oxides detected on the worn coating surfaces of the samples, together with the morphology of the transfer layers and the optical observation of oxide-rich regions and adhered material on the cylinder (Figs. 13 and 14), provides indirect but consistent evidence of Fe oxide layer formation on the counterpart and material transfer occurring at the sliding interface.

4. Conclusions

This study investigated the effect of WC/Co reinforcement content on the processability, microstructure, mechanical properties, and dry-sliding wear behavior of Stellite 21-based MMC coatings produced by Laser Directed Energy Deposition (L-DED). Based on the obtained results, the following conclusions can be drawn:

- Coating integrity was strongly affected by the WC/Co content and processing conditions. Dense and crack-free coatings with relative densities above 99% were successfully produced up to 20 wt% WC/Co through appropriate optimization of laser power and scanning speed. At 30 wt% WC/Co, cracking and partial delamination occurred under all investigated conditions, indicating a processability limit for the Stellite 21–WC/Co system.
- Increasing the WC/Co content promoted significant microstructural refinement. The coatings evolved from a predominantly dendritic CoCr-based matrix to a dendritic–cellular structure embedded within an increasingly continuous eutectic network enriched with ultrafine carbides. Unlike several Stellite 6-based MMC systems reported in the literature, no significant undissolved WC agglomerates were observed, indicating effective dissolution and redistribution of the reinforcement during L-DED processing.
- The microstructural refinement induced by WC/Co addition resulted in a substantial increase in hardness, from approximately 410 HV1 for unreinforced Stellite 21 to values exceeding 800 HV1 for the 20 wt% WC/Co coating. In addition to reinforcement content, the thermal conditions associated with the processing parameters influenced carbide precipitation and matrix refinement.
- Dry-sliding tests against AISI 52100 steel demonstrated a progressive improvement in tribological performance with increasing WC/Co content. The 20 wt% WC/Co coating exhibited reductions in steady-state coefficient of friction of approximately 15% and 24% under 30 N and 50 N, respectively, compared with unreinforced Stellite 21. Simultaneously, the specific wear rate decreased markedly, reaching values of $0.40 \pm 0.01 \times 10^{-6}$ $mm^3/N{\cdot}m$ and $0.58 \pm 0.06 \times 10^{-6}$ $mm^3/N{\cdot}m$ at 30 N and 50 N, respectively.
- The enhanced wear resistance was associated not only with the increased hardness of the MMC coatings, but also with the formation of stable oxide-based tribolayers during sliding. The refined eutectic microstructure and the homogeneous dispersion of ultrafine carbides improved the load-bearing capacity of the coatings, promoting tribolayer stability and reducing its fragmentation.
- Worn surface analyses revealed a dominant tribo-oxidative wear regime accompanied by localized adhesive wear. The cyclic formation, disruption, and re-formation of oxide-based transfer layers governed the wear behavior, in agreement with wear mechanisms previously reported for Stellite-based MMC coatings.

Overall, the results demonstrate that L-DED enables the fabrication of Stellite 21–WC/Co MMC coatings with a favorable combination of processability, microstructural refinement, and tribological performance up to 20 wt% WC/Co. Compared with conventional Stellite 6-based systems, the Stellite 21 matrix appears particularly promising for reducing crack susceptibility while maintaining excellent wear resistance, making these coatings attractive for advanced wear-resistant surface engineering applications.

CRediT authorship contribution statement

Chiara Gianassi: Writing – original draft, Investigation, Data curation. **Gianluca Di Egidio:** Writing – original draft, Formal analysis, Data curation. **Erica Liverani:** Writing – review & editing, Formal analysis, Conceptualization. **Alessandro Fortunato:** Supervision, Project administration, Funding acquisition.

Declaration of competing interest

The authors declare that they have no known competing financial interests or personal relationships that could have appeared to influence the work reported in this paper.

Data availability

Data will be made available on request.

References

[1] Y. Hu, W. Cong, A review on laser deposition-additive manufacturing of ceramics and ceramic reinforced metal matrix composites, Ceram. Int. 44 (17) (2018) 20599–20612, https://doi.org/10.1016/j.ceramint.2018.08.083.
[2] G. Wang, J. Zhang, R. Shu, S. Yang, High temperature wear resistance and thermal fatigue behavior of Stellite-6/WC coatings produced by laser cladding with co-coated WC powder, Int. J. Refract. Met. Hard Mater. 81 (2019) 63–70, https://doi.org/10.1016/j.ijrmhm.2019.02.024.
[3] Y. Wang, et al., Research progress on the wear resistance of key components in agricultural machinery, Materials 16 (24) (2023) 7646, https://doi.org/10.3390/ma16247646.
[4] D. Chioibasu, S. Mihai, C.M. Cotrut, I. Voiculescu, A.C. Popescu, Tribology and corrosion behavior of gray cast iron brake discs coated with Inconel 718 by direct energy deposition, Int. J. Adv. Manuf. Technol. 121 (7–8) (2022) 5091–5107, https://doi.org/10.1007/s00170-022-09646-7.
[5] Y. Zhao, et al., Steel-based brake disc laser cladding coating preparation method and brake performance study, Eng. Fail. Anal. 167 (2025) 108962, https://doi.org/10.1016/j.engfailanal.2024.108962.
[6] C. Gianassi, et al., Laser directed energy deposition of FeSi/SS 316L advanced bimetallic high-speed rotors: from material characterization to performance evaluation, Adv. Ind. Manuf. Eng. 11 (2025) 100175, https://doi.org/10.1016/j.aime.2025.100175.
[7] D.R. Feenstra, R. Banerjee, H.L. Fraser, A. Huang, A. Molotnikov, N. Birbilis, Critical review of the state of the art in multi-material fabrication via directed energy deposition, Curr. Opin. Solid State Mater. Sci. 25 (4) (2021) 100924, https://doi.org/10.1016/j.cossms.2021.100924.
[8] T. DebRoy, et al., Additive manufacturing of metallic components – process, structure and properties, Prog. Mater. Sci. 92 (2018) 112–224, https://doi.org/10.1016/j.pmatsci.2017.10.001.
[9] M. Ostolaza, J.I. Arrizubieta, A. Lamikiz, E. Ukar, Study of the flexural behaviour and bonding strength of WC-Co metal matrix composite coatings produced by Laser Directed Energy Deposition, Surf. Coat. Technol. 463 (2023) 129538, https://doi.org/10.1016/j.surfcoat.2023.129538.
[10] J. Vavřík, T. Hrbáčková, P. Salvetr, M. Brázda, Stellite coating deposited by directED energy deposition, Presentato Metal 2020 (2020) 822–826, https://doi.org/10.37904/metal.2020.3559.
[11] G. Lin, et al., Effect of process parameters on the dimension and morphology of laser cladded WC-Ni composite coatings prepared by picosecond laser surface texturing, Opt. Laser Technol. 198 (2026) 114874, https://doi.org/10.1016/j.optlastec.2026.114874.
[12] E. Liverani, A. Ascari, A. Fortunato, Multilayered WC–Co coatings by direct energy deposition-based cladding: effect of laser remelting on interface defects, Surf. Coat. Technol. 464 (2023) 129556, https://doi.org/10.1016/j.surfcoat.2023.129556.
[13] Z. Smoqi, J. Toddy, H. (Scott) Halliday, J.E. Shield, P. Rao, Process-structure relationship in the directed energy deposition of cobalt-chromium alloy (Stellite 21) coatings, Mater. Des. 197 (2021) 109229, https://doi.org/10.1016/j.matdes.2020.109229.
[14] D. Smith, P. Pickett, T. Grabowski, J. Thorpe, F. Azarmi, Mechanical properties of cobalt chromium alloy manufactured by direct energy deposition technology, J. Therm. Spray Technol. 34 (2–3) (2025) 674–689, https://doi.org/10.1007/s11666-024-01913-1.
[15] V. Humarán-Sarmiento, E. Martínez-Franco, C. Félix-Martínez, A.-I. García-Moreno, Directed energy deposition of Stellite 6/WC-12Co metal matrix

composite, Surf. Coat. Technol. 488 (2024) 131021, https://doi.org/10.1016/j.surfcoat.2024.131021.
[16] D. Bartkowski, A. Bartkowska, Wear resistance in the soil of Stellite-6/WC coatings produced using laser cladding method, Int. J. Refract. Met. Hard Mater. 64 (2017) 20–26, https://doi.org/10.1016/j.ijrmhm.2016.12.013.
[17] C. Félix-Martínez, J.M. Salgado-López, A. López-Martínez, L.D. García-Salas, J. González-Carmona, C.E. Cruz-González, Microstructure, hardness, and wear resistance at room and high temperature of Stellite-6/WC-6Co coatings deposited by laser cladding process, Int. J. Adv. Manuf. Technol. 130 (7–8) (2024) 3355–3371, https://doi.org/10.1007/s00170-023-12881-1.
[18] G.J. Xu, M. Kutsuna, Cladding with Stellite 6 + WC using a YAG laser robot system, Surf. Eng. 22 (5) (2006) 345–352, https://doi.org/10.1179/174329406X98430.
[19] M. Ostolaza, J.I. Arrizubieta, A. Queguineur, K. Valtonen, A. Lamikiz, I. Flores Ituarte, Influence of process parameters on the particle–matrix interaction of WC-Co metal matrix composites produced by laser-directed energy deposition, Mater. Des. 223 (2022) 111172, https://doi.org/10.1016/j.matdes.2022.111172.
[20] L. Tonelli, C. Martini, L. Ceschini, Improvement of wear resistance of components for hydraulic actuators: dry sliding tests for coating selection and bench tests for final assessment, Tribol. Int. 115 (2017) 154–164, https://doi.org/10.1016/j.triboint.2017.05.021.
[21] L. Ceschini, C. Chiavari, A. Marconi, C. Martini, Influence of the countermaterial on the dry sliding friction and wear behaviour of low temperature carburized AISI316L steel, Tribol. Int. 67 (2013) 36–43, https://doi.org/10.1016/j.triboint.2013.06.013.
[22] J. Williams, R. Dwyer-Joyce, Modern tribology handbook. 2: Materials, coatings, and industrial applications, in: Contact Between Solid Surfaces, CRC Press, Boca Raton, Fla., 2001, pp. 121–162, 2 vol.
[23] L. Tonelli, M.M.Z. Ahmed, L. Ceschini, A novel heat treatment of the additively manufactured Co28Cr6Mo biomedical alloy and its effects on hardness, microstructure and sliding wear behavior, Prog. Addit. Manuf. 8 (2) (2023) 313–329, https://doi.org/10.1007/s40964-022-00334-2.
[24] W.C. Oliver, G.M. Pharr, Measurement of hardness and elastic modulus by instrumented indentation: advances in understanding and refinements to methodology, J. Mater. Res. 19 (1) (2004) 3–20, https://doi.org/10.1557/jmr.2004.19.1.3.
[25] J.R. Davis, ASM International, A c. di, Nickel, cobalt, and their alloys, in: ASM Specialty Handbook, 1. printing, ASM International, Materials Park, Ohio, 2000.
[26] M. Liu, A. Kumar, S. Bukkapatnam, M. Kuttolamadom, A review of the anomalies in directed energy deposition (DED) processes & potential solutions - part quality & defects, Procedia Manuf. 53 (2021) 507–518, https://doi.org/10.1016/j.promfg.2021.06.093.
[27] T. Zhao, et al., Some factors affecting porosity in directed energy deposition of AlMgScZr-alloys, Opt. Laser Technol. 143 (2021) 107337, https://doi.org/10.1016/j.optlastec.2021.107337.
[28] M.M. Bakhshayesh, F. Khodabakhshi, M.H. Farshidianfar, Š. Nagy, M. Mohammadi, G. Wilde, Additive manufacturing of Stellite 6 alloy by laser-directed energy deposition: engineering the crystallographic texture, Mater. Charact. 207 (2024) 113511, https://doi.org/10.1016/j.matchar.2023.113511.
[29] A. Farnia, F. Malek Ghaini, J.C. Rao, V. Ocelík, J.Th.M. De Hosson, Tantalum-modified Stellite 6 thick coatings: microstructure and mechanical performance, J. Mater. Sci. 48 (1) (2013) 140–149, https://doi.org/10.1007/s10853-012-6805-4.
[30] C. Jiang, et al., On enhancing wear resistance of titanium alloys by laser cladded WC-Co composite coatings, Int. J. Refract. Met. Hard Mater. 107 (2022) 105902, https://doi.org/10.1016/j.ijrmhm.2022.105902.
[31] M. Hu, J. Tang, X. Chen, N. Ye, X. Zhao, M. Xu, Microstructure and properties of WC-12Co composite coatings prepared by laser cladding, Trans. Nonferrous Metals Soc. China 30 (4) (2020) 1017–1030, https://doi.org/10.1016/S1003-6326(20)65273-6.
[32] M. Shafizadeh, G.G. Yapici, Wear performance of additive-manufactured and heat-treated CoCrMo alloy, Mater. Lett. 405 (2026) 139761, https://doi.org/10.1016/j.matlet.2025.139761.